Computers, Materials & Continua

Tech Science Press

Doi:10.32604/cmc.2025.068242

ARTICLE

Integrated Discrete Cell Complexes and Finite Element Analysis for Microstructure Topology Evolution during Severe Plastic Deformation

Siying Zhu[1,#], Weijian Gao[2,#], Min Yi[1,2,*] and Zhuhua Zhang[1,2,*]

[1]Institute for Frontier Science & Key Lab for Intelligent Nano Materials and Devices of the Ministry of Education, Nanjing University of Aeronautics and Astronautics (NUAA), Nanjing, 210016, China

[2]State Key Lab of Mechanics and Control for Aerospace Structures & College of Aerospace Engineering, Nanjing University of Aeronautics and Astronautics (NUAA), Nanjing, 210016, China

*Corresponding Authors: Min Yi. Email: yimin@nuaa.edu.cn; Zhuhua Zhang. Email: chuwazhang@nuaa.edu.cn

[#]Equal Contribution

Received: 23 May 2025; Accepted: 03 July 2025; Published: 29 August 2025

ABSTRACT: Microstructure topology evolution during severe plastic deformation (SPD) is crucial for understanding and optimising the mechanical properties of metallic materials, though its prediction remains challenging. Herein, we combine discrete cell complexes (DCC), a fully discrete algebraic topology model—with finite element analysis (FEA) to simulate and analyse the microstructure topology of pure copper under SPD. Using DCC, we model the evolution of microstructure topology characterised by Betti numbers (β_0, β_1, β_2) and Euler characteristic (χ). This captures key changes in GBNs and topological features within representative volume elements (RVEs) containing several hundred grains during SPD-induced recrystallisation. As SPD cycles increase, high-angle grain boundaries (HAGBs) progressively form. Topological analysis reveals an overall decrease in β_0 values, indicating fewer isolated HAGB substructures, while β_2 values show a steady upward trend, highlighting new grain formation. Leveraging DCC-derived RVE topology and FEA-generated plastic strain data, we directly simulate the evolution and spatial distribution of microstructure topology and HAGB fraction in a copper tube undergoing cyclic parallel tube channel angular pressing (PTCAP), a representative SPD technique. Within the tube, the HAGB fraction continuously increases with PTCAP cycles, reflecting the microstructure's gradual transition from subgrains to fully-formed grains. Analysis of Betti number distribution and evolution reveals the microstructural reconstruction mechanism underpinning this subgrain to grain transition during PTCAP. We further demonstrate the significant influence of spatially non-uniform plastic strain distribution on microstructure reconstruction kinetics. This study demonstrates a feasible approach for simulating microstructure topology evolution of metals processed by cyclic SPD via the integration of DCC and FEA.

KEYWORDS: Microstructure topology; betti numbers; discrete cell complexes; finite element analysis; severe plastic deformation

1 Introduction

The production of ultrafine-grained (UFG) metallic materials, which exhibit enhanced mechanical strength, ductility, and functional properties, remains a central pursuit in materials science [1,2]. Among the most effective methods for achieving these fine microstructures are severe plastic deformation (SPD) techniques, including high-pressure torsion (HPT), equal channel angular pressing (ECAP), accumulative roll bonding (ARB), and parallel tube channel angular pressing (PTCAP). These techniques impose large plastic strains without significantly changing the overall geometry of the sample, facilitating the synthesis

of advanced materials with superior performance [3,4]. Microstructure design is critical for achieving exceptional properties, gradient structures enable strength-ductility synergy [5], UFG architectures facilitate room-temperature superplasticity [6], and nanograined oxides exhibit "superfunctional" photocatalytic behaviour for energy applications [7]. A key mechanism contributing to microstructure refinement during SPD is continuous dynamic recrystallisation (CDRX) [8,9]. Unlike discontinuous dynamic recrystallization (DDRX), another important mechanism in SPD, CDRX proceeds through gradual subgrain rotation and boundary migration, transforming low-angle grain boundaries (LAGBs) into high-angle grain boundaries (HAGBs). In face-centred cubic (FCC) metals such as copper, this mechanism leads to the formation of ultrafine grains without requiring distinct nucleation events. In addition to improving mechanical properties, the recrystallised microstructure enhances electrical and thermal conductivities by reducing dislocation densities and internal stresses, making SPD-treated copper alloys attractive for applications demanding both strength and conductivity [10,11]. However, DDRX operates through distinct nucleation and growth stages: new strain-free grains nucleate preferentially at prior grain boundaries or deformation heterogeneities, followed by boundary migration that consumes the work-hardened matrix. This process dominates in low-to-medium stacking fault energy materials where rapid boundary mobility enables abrupt microstructural reconstitution. However, SPD regimes rarely exhibit pure DDRX, instead, it persistently couples with CDRX [12,13].

Microstructure typically plays a pivotal role in determining the properties of polycrystalline materials [14–17], governed largely by the grain boundary network (GBN) which influences key characteristics such as strength, ductility, and conductivity [18–20]. A critical microstructural factor is the HAGB fraction, significantly affecting grain boundary sliding [21,22], dislocation movement [23,24], and strain accommodation [25]. Materials with higher HAGB fractions generally exhibit enhanced mechanical properties, as these boundaries effectively impede dislocation motion. Furthermore, grain and grain boundary (GB) connectivity critically influences material behaviour by determining stress transfer and diffusion pathways. Topological aspects including triple junctions (TJs), quadruple nodes (QNs), and their connectivity can provide deeper insight into microstructure property relationships [19,26–29]. Quantifying these factors enables a comprehensive understanding of how microstructural features collectively govern material performance and functionality. Advanced research methodologies integrate multiscale characterisation and computational modelling to decode GBN evolution, a cornerstone of SPD microstructural engineering [18,30,31]. In-situ techniques like Shear Diamond Anvil Cells (SDAC) coupled with synchrotron X-ray diffraction enable real-time tracking of GB-mediated phase transformations under extreme pressures [32]. Advanced microscopy, particularly transmission Kikuchi diffraction (TKD) and atom probe tomography (APT) quantifies three-dimensional GB segregation patterns and defect densities across GBNs, revealing how solute decoration governs boundary mobility and stability [33]. Computationally, phase-field models simulate disconnection dynamics in boundary migration [34], Monte Carlo methods can stochastically simulate GB migration during DDRX [35], while molecular dynamics predicts vacancy cluster formation at TJs [36]. Despite these advances, critical defects persist: sample size constraints limit statistical analysis of GBN heterogeneity, thermal instability triggers abnormal grain growth via boundary migration above 0.3 T_m, and contamination in surface SPD introduces impurity drag at boundaries that degrades corrosion performance [37,38]. Crucially, incomplete models of stress-coupled boundary migration and disconnection mobility hinder the predictive control of network topology—particularly in ultra-SPD regimes, where boundary-dominated processes give rise to exceptional properties such as room-temperature superplasticity. Despite significant advances in the understanding of grain refinement induced by SPD, quantitative modelling of the evolving microstructural topology, especially the structure of GBNs, remains insufficiently developed. Most existing models do not fully capture the topological complexity and connectivity of the evolving GBN. A deeper

understanding and the ability to predict topological invariants of GBNs can provide valuable insights into the microstructural states associated with plastic deformation and dynamic recrystallisation. The one-way macro-to-meso coupling is computationally efficient and physically grounded, offering extensibility to other materials and SPD processes.

Our previous work [28,39] developed a discrete method based on algebraic topology to simulate the two-dimensional (2D) and three-dimensional (3D) microstructure and GBN evolution during SPD, which is described in detail in the PhD thesis [40]. This method effectively captured the GB dynamics and topology changes within the material at the mesoscale, providing insights into the underlying mechanisms of microstructural refinement. In this work, we extend this approach by integrating the algebraic topology-based mesoscale model with finite element methods (FEM). In detail, the output from discrete cell complexes (DCC) analysis of mesoscale representative volume element (RVE), i.e., the microstructure topology parameters as a function of plastic strain, is utilized by the macroscopic FEM analysis to obtain the spatial distribution of microstructure topology and HAGB fraction in a copper tube under cyclic parallel tube channel angular pressing (PTCAP), which is a typical SPD technique, and it is proposed to be suitable for deforming cylindrical tubes to extremely large strains [41,42]. By integrating the mesoscale simulation results with macroscopic FEM analysis, this work aims to establish a multiscale framework that bridges microstructure topology evolution with the macroscopic analysis. This study adopts the Maximum Entropy Production Principle (MEPP) as a guiding framework for modelling the conversion from LAGBs to HAGBs, assuming that the microstructure evolves along the path of maximal entropy production, consistent with principles of nonequilibrium thermodynamics.

2 Discrete Cell Complexes Model

2.1 Microstructure Representation

Voronoi tessellations provide geometric realisations of combinatorial structures known as discrete cell complexes—collections of cells of various topological dimensions connected according to specific rules [43]. It is widely used in GB simulations due to their ability to model the microstructural geometry of polycrystalline materials. This approach provides a detailed representation of the grain structure, allowing for accurate analysis of phenomena such as GB migration, curvature-driven growth, and the role of TJs in microstructural evolution.

Specifically, the assemblies studied in this work are 3-complexes, which are cell complexes with a topological dimension of 3. These are composed of 3-cells (polygons representing material cells or "grains" constructed), 2-cells (faces representing GBs), 1-cells (edges representing TJs or triple lines), and 0-cells (vertices representing QNs), as it shown in Fig. 1. The topology of a cell complex is uniquely characterized by a set of matrices that encode the connectivity between cells of different dimensions, forming its algebraic representation. Algebraic representations facilitate the topological analysis of cell complexes [43] and have been increasingly applied to mathematical models of physical phenomena on discrete spaces [44,45]. They significantly streamline the calculations in this study. The Voronoi tessellation used in this work was generated using the open-source software *Neper* [46], a versatile tool specifically designed to model and generate representative microstructures in computational materials science.

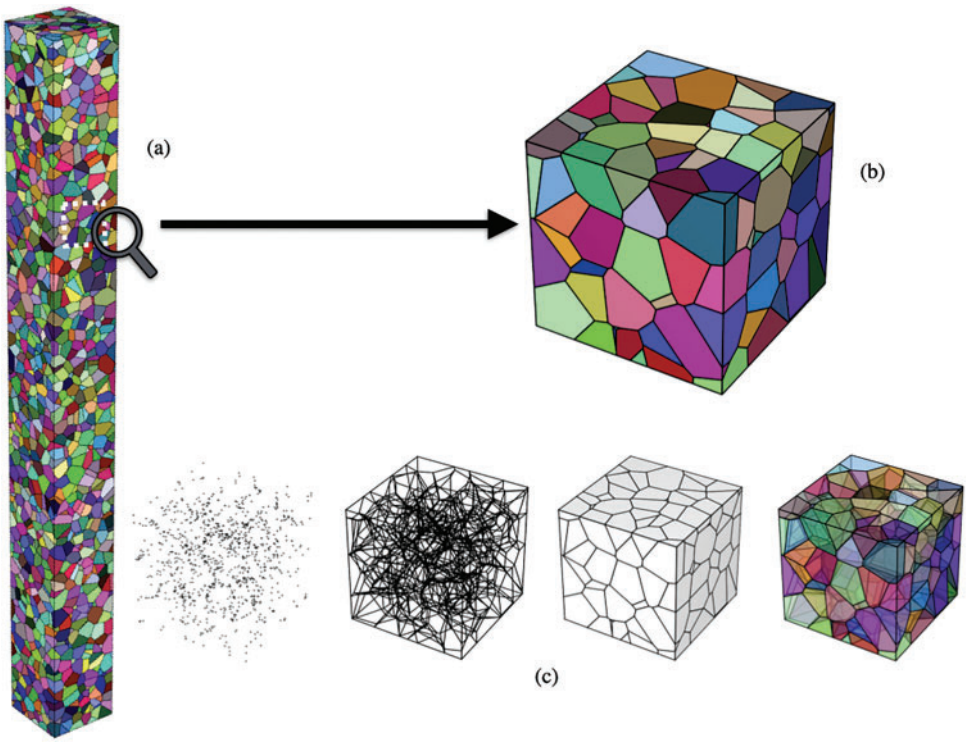

Figure 1: (**a**) 5000 cell Voronoi tessellation produced by *Neper*; (**b**) 200 cell Voronoi tessellation; (**c**) 3-complexes structure: 0-cells, 1-cells, 2-cells, 3-cells, from left to right

2.2 Discrete Cell Complexes

A collection of polyhedra, denoted by $\mathcal{M}$, serves as the geometric realization of a combinatorial construct known as a cell complex in algebraic topology [47]. Within this framework, a microstructure is characterized as a 3-complex, comprising cells of various dimensions. Specifically, a p-cell within $\mathcal{M}$ corresponds to a vertex, edge, polygonal face, or polyhedron for $p = 0, 1, 2, 3$, respectively, as illustrated in Fig. 1. The symbol σ_p denotes a p-cell, while N_p represents the total count of p-cells in $\mathcal{M}$. The relation $\sigma_p \prec \sigma_{p+1}$ implies that σ_p lies on the boundary of σ_{p+1}. A p-chain, denoted by C_p, refers to a formal linear combination of p-cells. The set of all such p-chains forms a vector space C_p, where the basis consists of the p-cells in the complex. Each cell is assigned a specific orientation. Commonly, a uniform orientation (e.g., outward-facing) is applied to all 3-dimensional cells, while orientations for lower-dimensional cells are assigned arbitrarily [48].

In an oriented discrete cell complex, the relationship between a σ_p and a σ_{p+1} cell can be classified into three types: (1) if σ_p is not on the boundary of σ_{p+1}, it is denoted by 0; (2) if $\sigma_p \prec \sigma_{p+1}$ and their orientations are aligned, the value is 1; and (3) if $\sigma_p \prec \sigma_{p+1}$ but their orientations are opposite, it is represented by -1. These relationships are encoded via boundary operators ∂_p for $p = 1, 2, 3$, which describe the topological structure of $\mathcal{M}$ and the operations performed on chains. The operator ∂_p maps p-chains to $(p-1)$-chains, i.e., $\partial_p : C_p \to C_{p-1}$, and obeys the fundamental property $\partial_{p-1} \circ \partial_p = 0$, implying that the boundary of a boundary is always null. From an algebraic perspective, ∂_p is expressed as a matrix with dimensions $N_{p-1} \times N_p$. Furthermore, $\partial_0 = 0$, since 0-cells (vertices) lack boundaries, and $\partial_4 = 0$, reflecting the fact that 3-cells are not the boundaries of any higher-dimensional cells. These boundary operators are also used to construct combinatorial Laplacians L_p, which map p-chains to p-chains, i.e., $L_p : C_p \to C_p$, for $p = 0, 1, 2, 3$.

And these are matrices of dimensions $N_p \times N_p$ is algebraically obtained by:

$$L_p = \partial_p^T \circ \partial_p + \partial_{p+1} \circ \partial_{p+1}^T. \tag{1}$$

Notably, $L_0 = \partial_1 \circ \partial_1^T$, and $L_3 = \partial_3^T \circ \partial_3$. Combinatorial Laplacians are used to compute different topological characteristics of the cell complex [49,50]. One example is the well-known Betti numbers, which are obtained simply by [51]:

$$\beta_p = \text{Dimension}(\text{Nullspace}(L_p)), \tag{2}$$

i.e., the number of zero eigenvalues of L_p. These have been used in many areas to characterize complex networks [27,52,53]. The alternating sum of Betti numbers gives the well-known Euler characteristic which separates topologically different structures, it provides the topological phase information for the HAGB substructure in our work:

$$\chi = \sum_{p\in\{0,1,2\}} (-1)^p \beta_p = \beta_0 - \beta_1 + \beta_2. \tag{3}$$

The positive value of $\chi > 0$ corresponds to the structures homotopically equivalent to the sphere; the structures with $\chi = 0$ equivalent to the torus, and in the last case of $\chi < 0$ corresponds to the most complicated case of several connected tori [54].

The set of all q-cells in $\mathcal{M}$, along with the lower-dimensional cells on their boundaries, is called the q-skeleton of $\mathcal{M}$, denoted by $\mathcal{M}_q$. Specifically: (1) $\mathcal{M}_3 = \mathcal{M}$; (2) $\mathcal{M}_2$ consists of all 2-cells, 1-cells, and 0-cells in $\mathcal{M}$; (3) $\mathcal{M}_1$ consists of all 1-cells and 0-cells in $\mathcal{M}$; (4) $\mathcal{M}_0$ consists of all 0-cells in $\mathcal{M}$. The Laplacians of $\mathcal{M}_q$ are computed using Eq. (1), with $\partial_{q+1} = 0$.

- For $\mathcal{M}_2$:

  $$L_0(\mathcal{M}_2) = \partial_0 \circ \partial_0^T \equiv L_0, \quad L_1(\mathcal{M}_2) = \partial_1^T \circ \partial_1 + \partial_2 \circ \partial_2^T \equiv L_1, \quad L_2(\mathcal{M}_2) = \partial_2^T \circ \partial_2 \neq L_2.$$

- For $\mathcal{M}_1$:

  $$L_0(\mathcal{M}_1) = \partial_0 \circ \partial_0^T \equiv L_0, \quad L_1(\mathcal{M}_1) = \partial_1^T \circ \partial_1 \neq L_1.$$

These Laplacians are used to compute the Betti numbers of the skeletons via Eq. (2). The Betti numbers considered here are:

- $\beta_0(\mathcal{M}_1) = \beta_0(\mathcal{M}_2)$: the number of disconnected components of 1-cells and 2-cells, quantifying the number of disconnected HAGB substructure.
- $\beta_1(\mathcal{M}_1)$: the number of one-dimensional holes, representing closed cycles of 1-cells, quantifying the number of "cycles" around HAGB substructure.
- $\beta_2(\mathcal{M}_2)$: the number of two-dimensional holes, representing closed cycles of 2-cells, quantifying the number of fully formed grains in HAGB substructure.

A substructure of a polycrystalline assembly consisting of elements of dimension q is a geometric realisation of $\mathcal{M}_q$. Consider a classification criterion that organizes the elements of the q-substructure into distinct sets based on their characteristics.

In this study, GBs are divided into a binary fashion—LAGBs and HAGBs, while TJs are classified into four types: J_0, J_1, J_2, and J_3, as illustrated in Fig. 2. Each category corresponds to a specific subset within $\mathcal{M}_q$,

and collectively, the union of these subsets reconstructs the entire set $\mathcal{M}_q$. The internal structure and orientation relationships within each subset are characterized using reduced boundary operators $\hat{\partial}_p$ (matrices) for $p = 1, 2, 3$. These operators encapsulate the local connectivity and orientation information of the elements in each group. By employing the general analytical framework previously introduced for $\mathcal{M}_q$, one can calculate topological invariants such as Laplacians, Betti numbers, and Euler characteristics corresponding to various q-substructures. The method adopted in this work focuses on analyzing substructures composed of the two GB types and the four TJ types. For example, the collection of HAGBs constitutes a subset of $\mathcal{M}_2$, and the second Betti number $\beta_2(\mathcal{M}_2)$ reflects the total number of grains in the polycrystalline structure, where a grain is defined as an enclosed region bounded entirely by HAGBs.

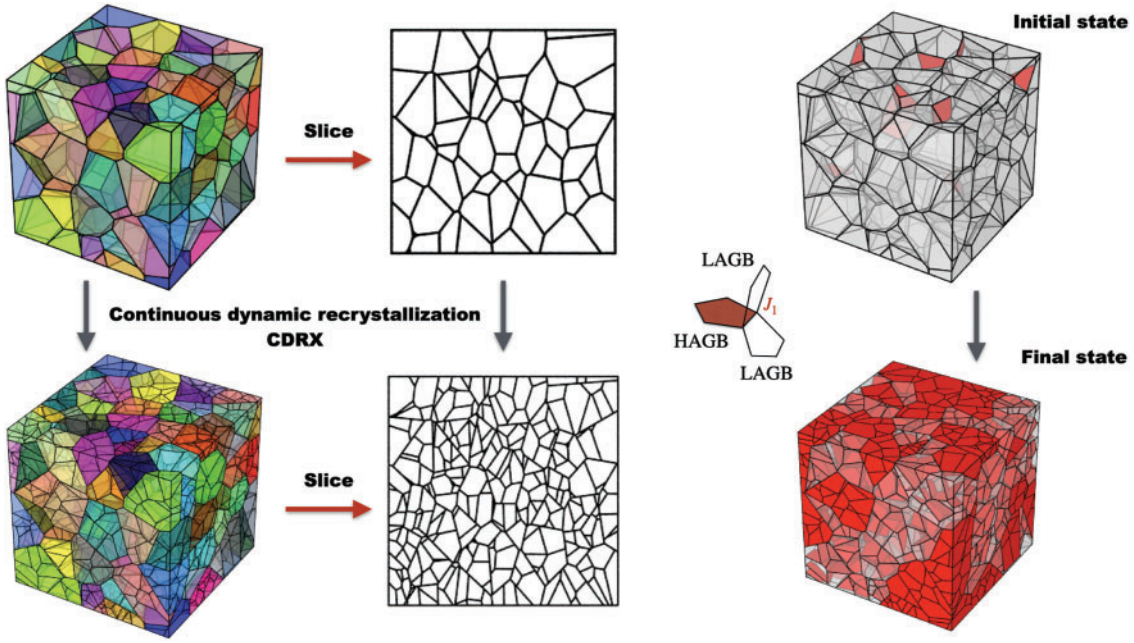

Figure 2: Schematic diagram of continuous dynamic recrystallisation and TJ type

2.3 Entropy and Grain Boundary Networks

Two types of entropy to characterize the properties of system from different perspectives are introduced. The first is the configurational entropy [39], derived from the spatial configuration of the system, and provides insight into the connectivity of the GBNs. Quantifies the degree of order or disorder in the arrangement of the network, effectively encoding the structural information of how GBs are connected. In a highly ordered structure, the configurational entropy is lower because there are fewer possible configurations, whereas in a disordered system, it is higher due to the greater number of possible arrangements, this measure captures the essence of the complexity and organization of the network. The entropy based on the TJ network referred to as the configurational or structural entropy, has been recently developed [19,39,55]. Let N_i be the number of TJs of type J_i, and $N = \sum N_i$ is the total number of TJs in a given complex. The configurational entropy S_J is defined by [39]:

$$S_J = -\sum_{i=0}^{3} j_i \log_2 j_i, \tag{4}$$

where $j_i = N_i/N$. The entropy defined by Eq. (4) is independent of the complex size, i.e., the number of polyhedrons to which a given domain is tessellated [39]. It is related directly to the system's information content and is formally equivalent to the standard definition of information entropy. Specifically, it measures the complexity of the TJ network, i.e., the amount of information required to describe it. Higher values of entropy indicate larger complexities. Since information entropy is typically measured in bits, the base of the logarithm in Eq. (4) is 2. Entropy determined with this base can be converted to any other required base.

Another one is the Euler entropy: $\chi = \sum_{p\in\{0,1,2\}}(-1)^p\beta_p$, based on the Euler characteristic. It is a topological invariant that provides global information about the shape and connectivity of a structure, it's particularly useful for analyzing changes in the topological phases of the system. This approach captures the global morphology and connectivity of HAGB substructures, enabling identification of topological phase transformations. When a network undergoes a phase transformation, such as merging or splitting of GBs, the Euler characteristic changes, reflecting the underlying shift in topology. The corresponding Euler entropy encapsulates this transformation, offering a complementary perspective to configurational entropy by focusing on the system's topological transitions rather than its connectivity details.

Together, these two types of entropy provide a comprehensive framework for understanding both the structural and topological aspects of GBNs, bridging local connectivity with global topological behaviour. The maximum entropy production principle (MEPP) is applied as the evolution principle in this simulation according to TJ configurational entropy. MEPP was independently proposed in various fields of physics in the mid-20th century [56] and has proven highly effective in analyzing a wide range of non-equilibrium phenomena [57,58]. This approach builds on prior work [57,59], in particular, the method proposed in [59] provides the theoretical foundation for our formulation. Algorithmically, it is implemented by assigning entropy production weights to discrete cell transitions within the network. The initial GBN begins in a state where only 0.05% of its boundaries are classified as HAGBs, these HAGBs are dispersed throughout the microstructure in a random spatial configuration, while the remaining 99.95% of boundaries are LAGBs, as it shown in Fig. 2. During the evolution of the GBN, the system undergoes a dynamic reorganization process driven by MEPP: at each step, the microstructure selectively transforms LAGB into HAGB in a manner that optimizes the entropy of the entire network; This transformation prioritizes boundaries whose conversion to HAGBs would result in the greatest increase in configurational disorder; Finally, no further transformations of LAGBs to HAGBs, meaning the microstructure achieves a stable energy-minimized state where the spatial distribution and proportion of HAGBs remain constant.

Fig. 3 illustrates the evolution of the GBN with increasing fraction of HAGBs according to MEPP based on TJ configurational entropy and topological metrics. Fig. 3a shows the configurational entropy S_J, which follows a parabolic trend. Starting from the initial state (dominated by LAGBs), S_J increases as the fraction of HAGBs grows, reaching a maximum when the GBN approaches an equilibrium configuration. Beyond this point, S_J decreases as the network becomes increasingly dominated by HAGBs, representing the decrease of the GBN complexity. Fig. 3b presents the evolution of Euler entropy $\ln(\chi(f))$ and the inverse connectivity ratio β_0/β_2. The Euler entropy $\ln(\chi(f))$ exhibits an increasing trend during the initial evolution, and appeared the first topological phase transformation around $f = 0.043$. Declines sharply as the system approaches a state dominated by HAGBs. At approximately $f = 0.728$, the second topological phase transformation occurs, indicating a transition in the underlying topological structure from a "torus" to a "sphere" in the topological space. This phase transformation reflects a fundamental change in the connectivity and geometry of the GBN. In algebraic topology, such transitions are characterized by changes in the Betti numbers β_0, β_1 and β_2, which represent the number of disconnected components, one-dimensional holes (cycles) and two-dimensional voids (number of grains in GBN), respectively. As the system evolves, the reduction in β_0 and β_1, the increase in β_2 signifies the collapse of lower-dimensional

holes and the construction of higher-dimentional holes of the network structure. This transition aligns with the broader principle of entropy production, where the system shifts toward a more stable and less geometrically complex configuration dominated by HAGBs. $\ln(\beta_0/\beta_2)$, which represents the inverse connectivity, decreases initially, indicating a more connected network structure, and increases later as the network becomes fragmented. Together, these metrics highlight the transition from a predominantly LAGB network to a more fragmented HAGB-dominated structure, governed by the MEPP.

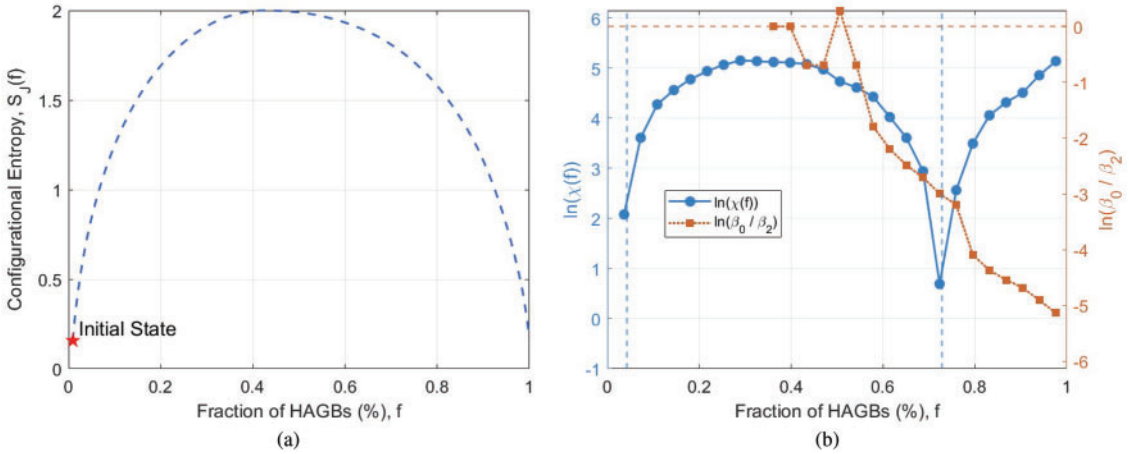

Figure 3: (**a**) Evolution of configurational entropy $S_J = -\sum_{i=0}^{3} j_i \log_2 j_i$ obtained by maximum entropy production principle; (**b**) Evolution of Euler entropy $\chi = \sum_{p\in\{0,1,2\}} (-1)^p \beta_p$ and inverse connectivity β_0/β_2 obtained by maximum entropy production principle

2.4 Evolution of Betti Numbers and Euler Characteristics

The evolution of topological characteristics in the GBN is analyzed through Betti numbers $\beta_0, \beta_1, \beta_2$ and the Euler characteristic χ, as a function of the fraction of HAGBs in Fig. 4.

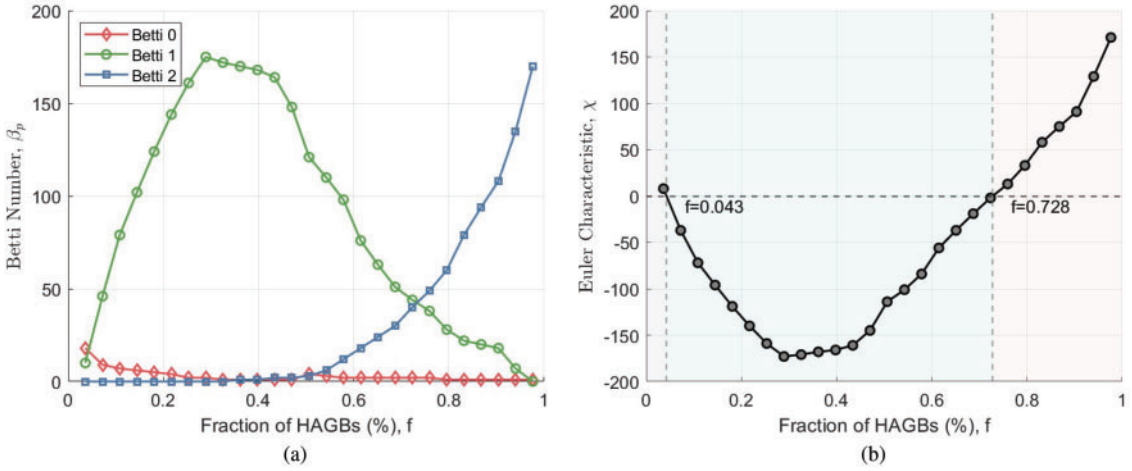

Figure 4: (**a**) Evolution of Betti numbers $\beta_0, \beta_1, \beta_2$ obtained by maximum entropy production principle; (**b**) Evolution of Euler characteristic χ obtained by maximum entropy production principle

Fig. 4a shows the behaviour of the Betti numbers. β_0 (red curve), which represents the number of disconnected components of HAGB network, decreases slightly at first and then remains relatively constant throughout the increase in HAGBs, reflecting a stable connectivity of the network. β_1 (green curve), which represents the number of independent 1-cycles along the HAGBs surface, increases sharply, peaking near a fraction of 0.4, indicating the formation of more loops in the 3D GBN. Beyond this point, β_1 declines, signifying the breakdown of loops as the HAGBs continue to dominate. β_2 (blue curve), which corresponds to the number of grains, starts at a low value, increases steadily until approximately 60% of HAGBs, and then rises sharply as the network transitions to a phase dominated by grain structures defined entirely by HAGBs. Fig. 4b presents the Euler characteristic χ, which represents the global topology of the GBN. Initially, χ is positive, indicating a dominance of grains with relatively fewer loops. As the fraction of HAGBs increases, χ decreases, becoming negative around a fraction of 0.2 and reaching its minimum near 0.4 of HAGB fraction. This transition highlights a shift to a topology with more complex connectivity and a higher number of loops. Beyond this point, χ starts to increase, eventually crossing zero at approximately 0.726, marking a topological phase transformation. As the HAGBs approach full dominance, χ becomes positive again, indicating a simpler topology dominated by grains with reduced loop complexity.

The interplay between Betti numbers and the Euler characteristic across varying HAGB fractions demonstrates the intricate relationship between local features (e.g., loops and grains) and global topological phases, providing valuable insight into the structural evolution of the GBN.

2.5 Evolution with Accumulated Plastic Strain

The relationships between network invariants and the HAGB fraction discussed earlier provide one aspect of the structural evolution during SPD, and the connection between the HAGB fraction and the accumulated plastic strain, $f(\varepsilon)$, where ε represents the accumulated plastic strain, is equally important. This relationship acts as a material- and process-dependent mapping that links experimentally measured strain to the experimentally determined HAGB fraction, reflecting the microstructural changes induced by SPD. The evolution of the HAGB fraction in copper alloys subjected to SPD has been extensively studied and reported in several works, such as [55,59]. As strain accumulates during SPD, the proportion of HAGBs increases due to mechanisms such as grain subdivision, dislocation activity, and dynamic recrystallisation. These processes fragment the original LAGBs and convert them into HAGBs, which play a pivotal role in enhancing material properties, such as strength and hardness, through grain refinement.

Experimental evidence highlights a consistent trend that the HAGB fraction starts at a low value in the undeformed material and progressively rises with increasing plastic strain until saturation is reached at high strains. This evolution provides valuable insights into the GBN's ability to accommodate deformation. In [55], a mathematical relationship to describe the dependence of the HAGB fraction f on the accumulated plastic strain ε is proposed, offering a framework to predict microstructural transformations under different SPD conditions:

$$f = \frac{\sqrt{a}\exp(a\varepsilon)}{\sqrt{1+b\exp(2a\varepsilon)}} + c\ln(1+\varepsilon) - \sqrt{\frac{a}{1+b}}, \tag{5}$$

here, a, b, c are dimensionless material parameters. The derivation of Eq. (5) is based on a statistical approach, where the fraction of HAGBs, f, is treated as an order parameter. This allows the application of the Landau formalism [60] to describe the evolution of f during deformation. The parameters a, b, c are coefficients in the differential equation $df/d\varepsilon = af - bf^3 + cf^6$, which is derived from the expansion of the free energy $F(f)$ in powers of f. These coefficients govern the behaviour of f as a function of strain and encapsulate the material's response to plastic deformation. The specific values of a, b, c are determined by fitting Eq. (5)

to experimental data, ensuring that the model accurately captures the evolution of the HAGB fraction for different materials under various processing conditions. While this form can be theoretically motivated, it also serves as an effective empirical descriptor of microstructure evolution in SPD processes, adaptable across various copper alloys.

The curve fitting for various copper alloys, aligning the experimental data with the proposed equation for the evolution of the HAGB fraction is illustrated in Fig. 5a. The curves demonstrate how the material parameters a, b, c capture the unique response of different alloys to accumulated plastic strain, reflecting the progressive transition of GBNs during SPD. In Fig. 5b, the corresponding changes in the GBN topological characteristics are highlighted, marked by changes in the Euler characteristic. These topological structure transitions, driven by mechanisms such as grain subdivision and recrystallisation, correlate directly with the increase in HAGB fraction, offering a comprehensive view of the microstructural and topological transformations occurring during the SPD process.

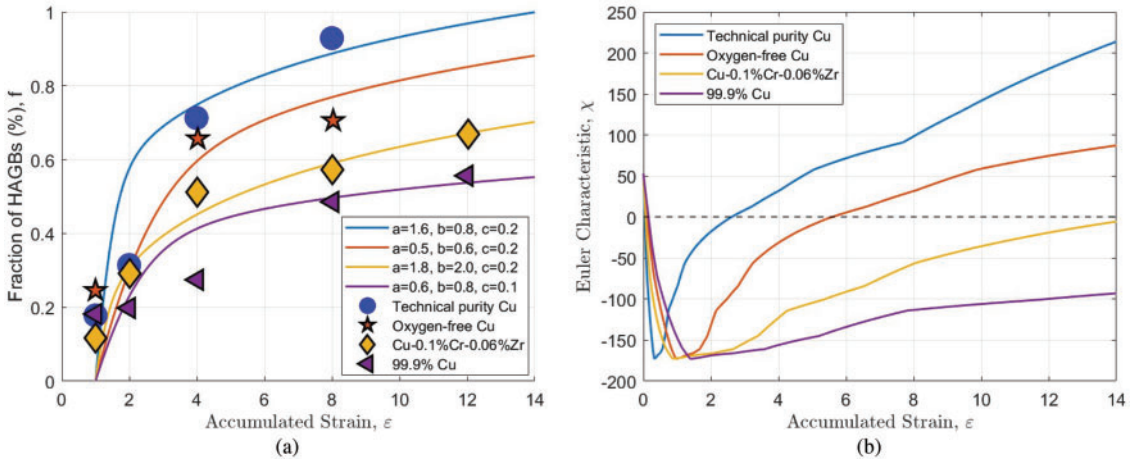

Figure 5: (**a**) Fraction of HAGBs p as function to accumulated plastic strain ε for copper alloys processed by PTCAP; (**b**) Evolution of Euler characteristic with accumulated plastic strain ε

3 Finite-Element Analysis for Topology Evolution during Cyclic SPD

PTCAP is a typical SPD technique. Compared to the widely employed Equal Channel Angular Pressing (ECAP) process, PTCAP offers the advantage of facilitating multiple deformation cycles with greater ease, thereby enabling higher levels of accumulated plastic strain (PEEQ). The primary components of the PTCAP setup comprise the punch, die, mandrel, and tube, with the structural schematic depicted in Fig. 6a. In practical applications, following each PTCAP operation, the specimen is typically rotated and inverted before the subsequent compression step. This complete sequence constitutes a single PTCAP cycle, as illustrated in Fig. 6b. According to our previous study [39], a sufficiently wide range of PEEQ is essential to capture the microstructural evolution of copper fully. Consequently, to explore the topological development of copper microstructure during the PTCAP process, numerical simulations were performed using the commercial finite element software *Abaqus*. To ensure adequate strain accumulation, four successive PTCAP cycles were simulated. The DCC method was subsequently employed to systematically examine the evolution of copper microstructural topology as a function of PEEQ.

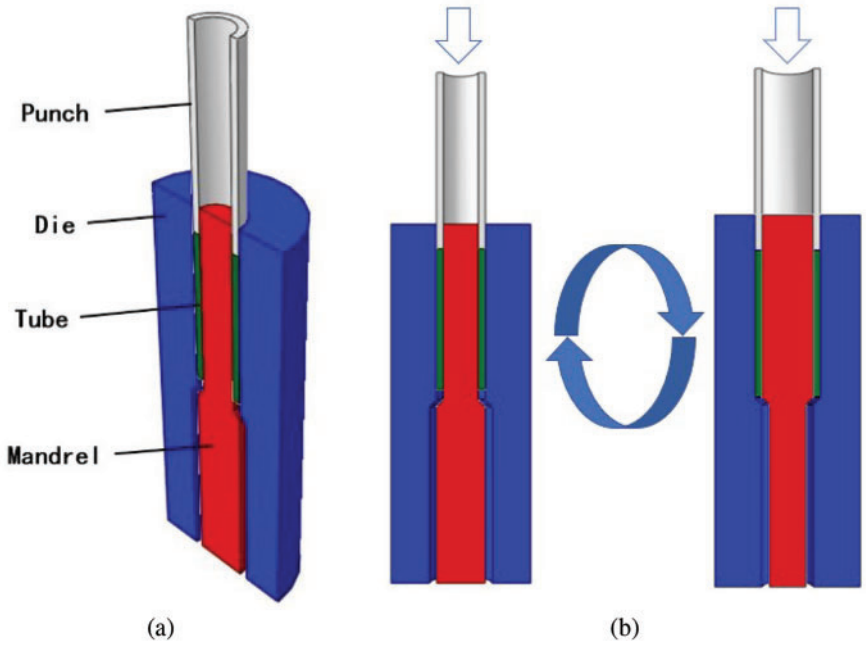

Figure 6: (**a**) Schematic diagram of PTCAP structure; (**b**) Schematic diagram of multiple PTCAP processes

3.1 Finite-Element Simulation Details

Owing to the symmetry in the geometry, material properties, and boundary conditions of the simulated object, an axisymmetric model was adopted during the modelling process. This approach significantly simplified both the model's construction and the subsequent analysis. As illustrated in Fig. 7, the components shown in the assembly diagram comprise the punch (a), mandrel (b), tube (c), and die (d). Of these, the punch, die, and mandrel were defined as discrete rigid bodies, whereas the tube was modelled as a deformable body.

As this study does not focus on the geometric optimisation of the PTCAP tooling, the die channel angle and radius were set according to the values reported in [61]. The research in this paper suggests that larger channel angles permit greater strain accumulation over the same number of cycles. However, in numerical simulations, larger angles may result in excessive mesh distortion, which in turn compromises convergence and the accuracy of the results. To balance the need for effective strain accumulation with numerical stability, a channel angle of 135° was ultimately selected in this study (Table 1). Furthermore, it has been observed that increasing the difference in radius between the inlet and outlet channels—effectively expanding the deformation—can also enhance the maximum accumulated equivalent plastic strain within a given number of cycles. While higher deformation contributes positively to strain accumulation, the improvement is relatively modest. Taking into account both computational efficiency and forming quality, the deformation was set to 2 mm in this study (Table 1). As shown in Table 1, the mandrel features a stepped geometry, with a radius of 5 mm at the thinner section and 7 mm at the thicker section. The tube has a wall thickness of 2 mm and an overall length of 40 mm. It is composed of commercially pure copper, characterised by a density of 8.1×10^{-9} ton/mm^3, Young's modulus of 1.1×10^5 MPa, and a Poisson's ratio of 0.33. The plastic constitutive behaviour is modelled using the Johnson-Cook constitutive equation which is expressed as:

$$\sigma = \left(A + B\varepsilon^n\right)\left[1 + C\ln\left(\frac{\dot{\varepsilon}}{\dot{\varepsilon}_0}\right)\right]\left[1 - \left(\frac{T - T_r}{T_m - T_r}\right)^m\right] \tag{6}$$

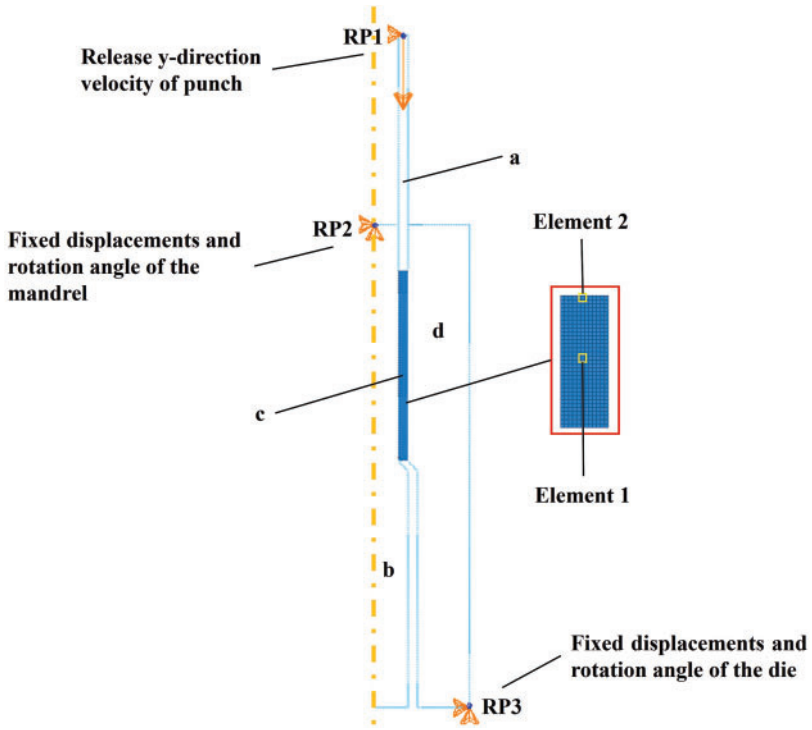

Figure 7: Loading and boundary condition for an axisymmetric finite-element model of PTCAP processing of copper tube

Table 1: Values of geometric parameters and process parameters

Parameters name	Units	Values
Short radius of mandrel	mm	7
Long radius of mandrel	mm	5
Deformation rate	mm	2
Change angle	°	135
Thickness of tube	mm	2
Length of tube	mm	40
Young's modulus	MPa	1.1×10^5
Density	ton/mm^3	8.1×10^{-9}
Poisson's ratio		0.33
Friction coefficient		0.05
Loading speed	mm/s	1

In the above equation, A, B, C, n and m are material constants; ε is the equivalent plastic strain; $\dot{\varepsilon}_0$ is the reference strain rate; T is the test temperature; T_r is the room temperature; and T_m is the material's melting temperature. The calibration of Johnson-Cook parameters of a material is beyond the scope of the current work. The selection of these parameters was informed by the findings reported in [62], in which the simulated stress-strain curves under various temperatures and strain rates were compared with experimental data. The comparison confirmed that the chosen parameters accurately represent the mechanical behaviour of

fine-grained T2 pure copper under high-temperature and high strain rate conditions, thereby demonstrating the suitability and reliability of the model parameters. The specific values are listed in Table 2.

Table 2: The values of J-C constitutive parameters for pure copper

A/MPa	B/MPa	C	n	m	T_r/°C	T_m/°C	$\dot{\varepsilon}_0/s^{-1}$
50	312.4	0.0438	0.3572	0.6261	25	1083	0.00222

Given the substantial deformation occurring during the PTCAP process, this study employed a dynamic explicit analysis step to simulate four successive PTCAP cycles. To mitigate mesh distortion resulting from severe deformation—which could compromise the accuracy of the results—the Arbitrary Lagrangian-Eulerian (ALE) adaptive meshing technique was activated. Furthermore, to accelerate the computational process, mass scaling was applied with a scaling factor of 1,000,000. In terms of contact definitions, face-to-face contact was established between the copper tube and the die, the mandrel, and the punch, respectively. Self-contact was also defined for the copper tube to account for potential internal interactions during deformation. To avoid geometric interference, the normal contact behaviour was defined as hard contact, while the tangential behaviour was governed by a penalty contact formulation. A friction coefficient of 0.05 was employed in (Table 1), in line with values reported in [61]. This value also ensures consistency with other selected process parameters—such as the channel angle, deformation (determined by the radius difference between inlet and outlet channels), and loading speed, thereby effectively controlling experimental variables. Reference points RP1, RP2, and RP3 corresponded to the die, mandrel, and punch, respectively. About boundary conditions, all translational and rotational degrees of freedom were constrained for RP2 and RP3, while RP1 was constrained in all directions except for translation along the Y-axis. Also according to [61], an increased loading rate significantly enhances the accumulation of equivalent plastic strain (PEEQ) during a single PTCAP cycle. However, elevated loading rates may also lead to substantial heat generation due to frictional effects, thereby introducing thermal influences. As thermal-mechanical coupling was not considered in the present numerical simulations, a conservative loading rate of 1 mm/s was selected to minimise errors arising from temperature rise and reduce the influence of thermal effects on simulation accuracy (Table 1). The copper tube was meshed using CAX4R elements. In contrast, rigid components were meshed using RAX2 elements.

The flowchart and coupling schemes of the integrated framework are summarised in Fig. 8, illustrating how the real GBN, DCC model and FEA simulation work together. In the present framework, the DCC serves as a topologically faithful representation of the polycrystalline microstructure, and this abstraction enables a discrete but physically interpretable mapping of the GBN evolution during SPD. The evolution of microstructure under SPD, including subgrain rotation to boundary misorientation accumulation and grain fragmentation, is reflected as topological transformations within the DCC. The conversion of LAGBs into HAGBs corresponds to increased connectivity and loop formation in the DCC, which are quantitatively characterised by changes in Betti numbers and the Euler characteristics.

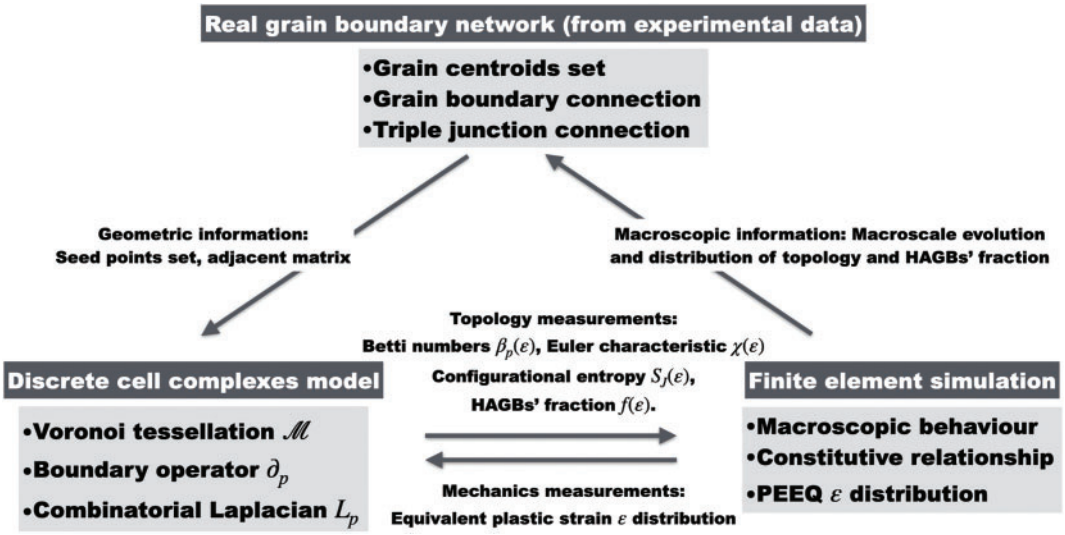

Figure 8: Flowchart and coupling schemes

3.2 Finite-Element Simulations Results

Through finite-element simulations, the PEEQ (equivalent plastic strain) data ε of the copper tube during four PTCAP cycles can be obtained. Based on the previous output that correlates HAGB fraction, entropy and topological descriptors with PEEQ from Section 2, a Python script is coded to map the PEEQ values at each integration point and calculate the corresponding values of HAGB fraction, entropy and topological descriptors. This section presents contour maps showing the spatial distribution of various parameters, i.e., HAGB fraction (f) shown in Fig. 9, Betti numbers ($\beta_0, \beta_1, \beta_2$) shown in Fig. 10, throughout different PTCAP cycles (from cycle 1 to 4). To enhance the visual clarity, uniform display thresholds are applied.

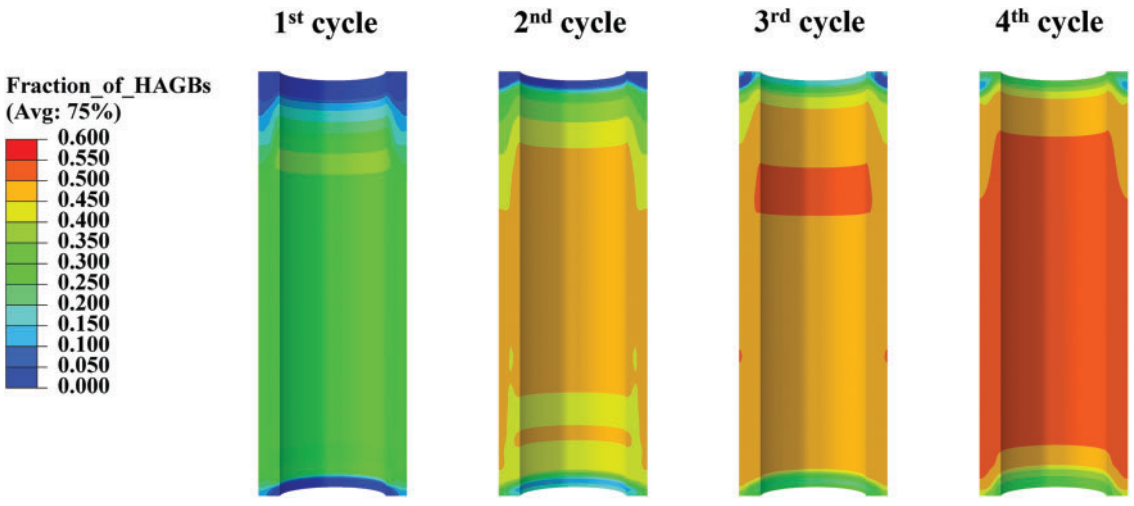

Figure 9: Contour maps for the HAGB fraction distribution after each PTCAP cycle

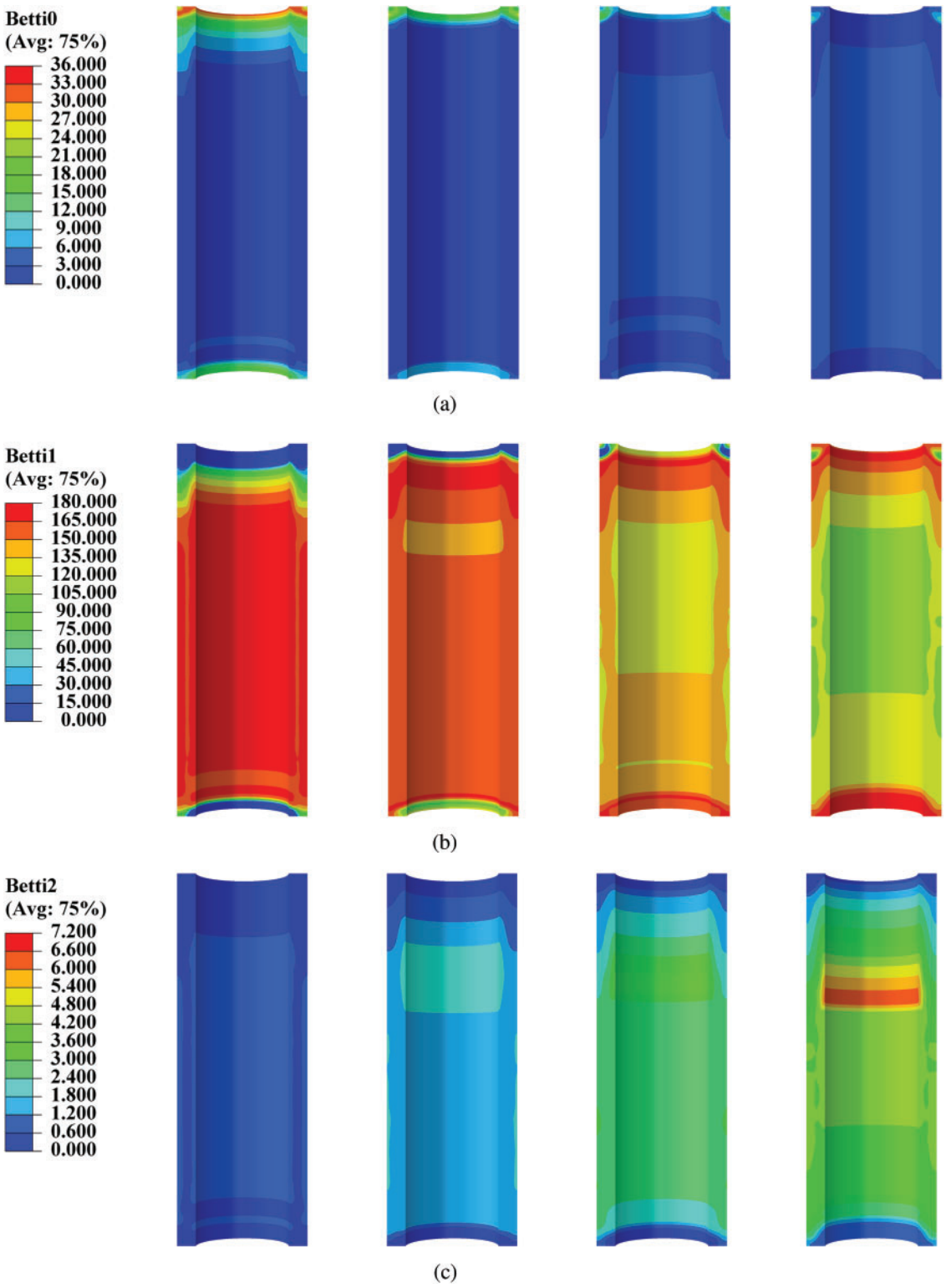

Figure 10: Contour maps for the distribution of microstructure topology parameters after each PTCAP cycle: (**a**) Betti0 (β_0); (**b**) Betti1 (β_1); (**c**) Betti2 (β_2)

The current framework employs a one-way coupling scheme from FEA to microstructural evolution. In this approach, the macroscopic strain and stress fields obtained from FEA are used as inputs to drive the topological evolution of the GBN, without accounting for feedback effects from the evolving microstructure on the mechanical response. This assumption is justified within the scope of the present study, which aims to establish a tractable method for investigating topological descriptors such as Betti numbers, Euler characteristics, and HAGB fractions under SPD. The one-way strategy offers computational efficiency and preserves a clear separation of scales, while still capturing the essential features of microstructural evolution. It captures key aspects of GBN evolution, including the progressive transformation of LAGBs into HAGBs and the restructuring of TJs. However, it does not currently model the explicit coalescence or splitting of GBs. While interactions among multiple grains are embedded within the topological structure of the DCC, dynamic reconnections or local topological changes, such as grain fragmentation or merging, remain beyond the scope of this work.

In Fig. 9, it is found that with increasing PTCAP cycles, the HAGB fraction in the copper tube gradually increases, primarily due to the CDRX mechanisms that promote the transformation of LAGBs into HAGBs, indicating that subgrains are progressively transformed into grains and new grains form. In tube-shaped PTCAP samples, the distribution of HAGBs is often heterogeneous, influenced by the imposed shear strain gradient across the cross-section, with a higher concentration typically observed near the outer wall where strain is most intense. While traditional metrics such as grain size distribution and average HAGB fraction offer limited insight into the topological structure of evolving GBNs, higher-order metrics such as the distribution of triple junction types, can capture essential features of topological change. These features, accessible via EBSD and previously validated in our earlier work [28,39], offer a meaningful way to compare simulated and experimental microstructures in the context of SPD-induced grain refinement. Fig. 10 illustrates the spatial evolution of microstructural topology in the PTCAP-processed tube samples through contour maps of Betti numbers β_0, β_1, and β_2 after each deformation cycle. β_0 shown in Fig. 10a maps reveals a progressive decrease in the number of connected components, particularly in the outer regions of the tube, indicating increased HAGB structure connectivity with continued deformation. β_1 can quantify the number of one-dimensional loops or holes, and initially shows high values concentrated near the edge regions, where plastic strain is most intense. These regions become more uniformly distributed and exhibit reduced β_1 magnitudes in later cycles, suggesting a simplification of the HAGB network due to the annihilation of loops, as shown in Fig. 10b. β_2 representing two-dimensional enclosed voids (fully formed grain), remains low in the early cycles but increases slightly in the mid-to-late stages, particularly in the central region, as shown in Fig. 10c.

As it shown in Fig. 11, to elucidate the heterogeneous microstructural evolution induced by PTCAP, the development of HAGB networks was analyzed at two representative FE points: one situated in the central region of the tube—Element 1, and the other at the center of the edge region—Element 2. These points experience markedly different strain paths and magnitudes due to the inherent strain gradient imposed by the PTCAP die geometry and sample curvature. The FE Element 2 is subjected to higher PEEQ, promoting more pronounced grain fragmentation and a faster transformation from LAGBs to HAGBs via CDRX. In contrast, the central region Element 1, characterized by lower strain accumulation and a more uniform stress state, exhibits a slower HAGB formation rate and retains a higher fraction of LAGBs throughout processing.

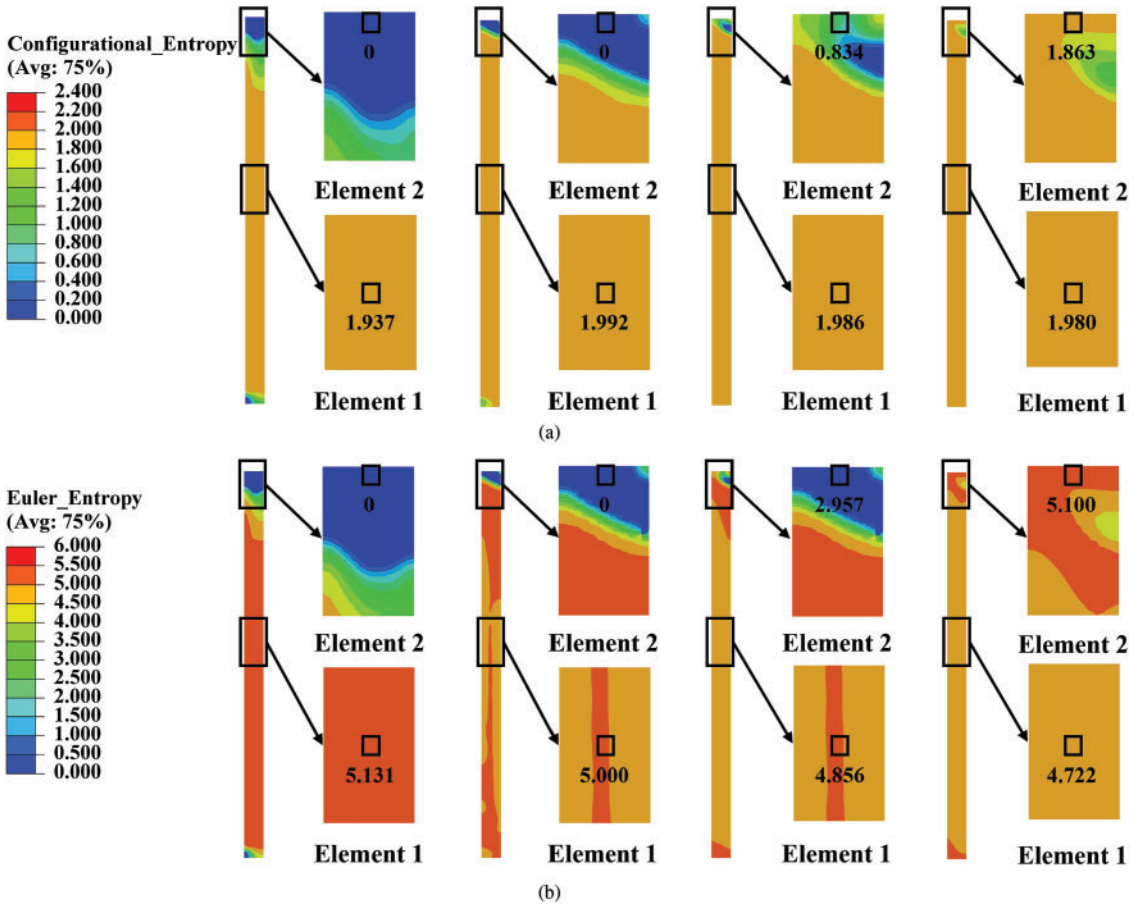

Figure 11: Contour maps for the distribution of two types of entropy after each PTCAP cycle and the difference between Elements 1 and 2: (**a**) Configurational entropy; (**b**) Euler entropy

To capture the local topological evolution of the microstructure under SPD, a representative, referred to as FE element 1, was selected for detailed analysis. The evolution of configurational and Euler entropy at FE Element 1 can provide complementary insights into the structural reorganization of the HAGB network during PTCAP processing, as it shown in Fig. 12a. Both entropy measures reveal significant changes in GBN structure as the PEEQ increases. Notably, the configurational entropy rises with increasing strain but tends to plateau once PEEQ ≈ 3, suggesting that the overall disorder or randomness in GB misorientation stabilizes beyond this strain level. In contrast, the Euler entropy continues to exhibit a gradual decline even after PEEQ = 3, indicating ongoing changes in the topological features of the HAGB network. This divergence implies that while the configurational complexity of the GBN becomes saturated, the underlying connectivity and spatial organization of HAGBs captured by Euler characteristics continues to evolve. These findings suggest a decoupling between misorientation-driven disorder and the GBN's topological structure, highlighting that topological descriptors provide essential and distinct information beyond conventional crystallographic metrics in characterizing microstructural evolution under severe plastic deformation.

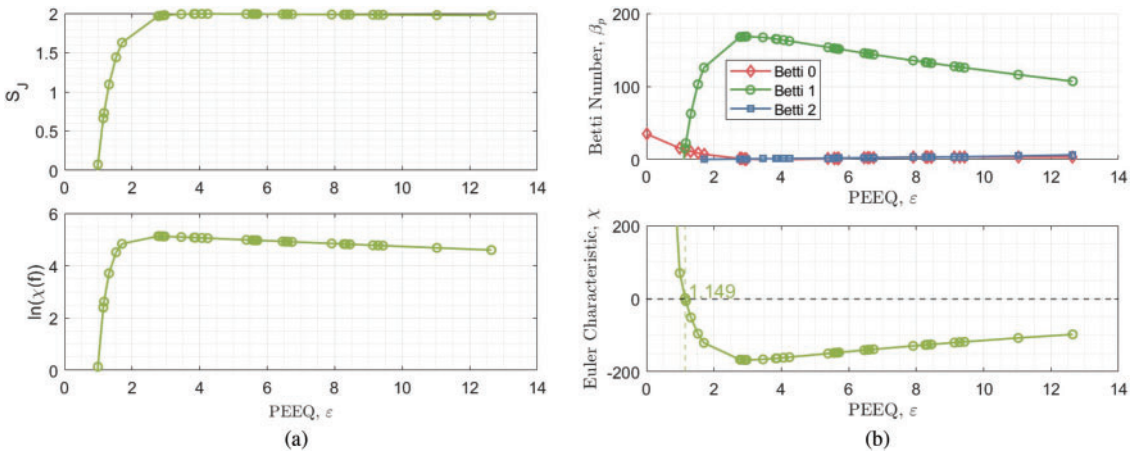

Figure 12: (**a**) Configurational entropy and Euler entropy as functions of the PEEQ of Element 1; (**b**) Betti numbers and Euler characteristic as functions of the PEEQ of Element 1

Changes in Betti numbers further elucidate the dynamic microstructure topology evolution in Fig. 12b with the evolution of HAGB network. β_0 decreases rapidly during the initial stage, indicating a substantial reduction in isolated topology components as connections form among subgrains. β_1 reaches a peak at PEEQ $\varepsilon \approx 3.0$, corresponding to the maximum number of closed GB loops and marking the peak of grain reconfiguration. Thereafter, β_1 gradually declines, while β_0 exhibits a slight rebound before decreasing again, suggesting that some looped structures rupture or merge into newly formed grains. β_2 shows a steady upward trend throughout the process, reflecting an increase in cavities or enclosed regions within the three-dimensional structure. This indicates the nesting or splitting of topological loops that have not yet fully evolved into grains, pointing to a progressive increase in structural complexity. Fig. 12b presents the trend of Euler characteristic, closely aligning with the aforementioned topology indicators. As PEEQ increases, the Euler characteristic rapidly decreases from a positive to a negative value, signifying enhanced connectivity and a substantial increase in topology complexity. In the early stage, the formation of numerous topology loops contributes to this decline. During the mid-to-late stages, the Euler characteristic gradually stabilizes and exhibits a slight rebound, suggesting that some topology voids are filled or the structure undergoes rearrangement, leading to a more ordered microstructure.

4 Conclusions

In conclusion, we have integrated macroscopic FEA and mesoscopic DCC analysis to demonstrate the attempt for the computational evaluation of the microstructure topology evolution during PTCAP cycles that belong to a typical SPD process. Microstructure topology evolution (HAGB fraction, Betti numbers, Configurational/Euler entropy, and Euler characteristic) in the RVE including microstructure details is predicted by DCC simulations. The macroscopic deformation behaviour under PTCAP cycles is simulated by FEM with a Johnson-Cook constitutive relationship to obtain PEEQ distribution. These simulations are one-way coupled through the information transfer among them. Microstructure topology parameters as functions of accumulated strain PEEQ are used as input for the FEA. In detail, once PEEQ is calculated at the FE node, microstructure topology parameters at this corresponding node are determined by the DCC simulation results and thus their spatial distribution is readily presented in the macroscopic scale.

Using the mesoscopic DCC analysis of copper RVE, the microstructure topology evolution as a function of accumulated strain is explored during the SPD process. The progressive increase in the HAGB faction

indicates CDRX, where subgrains transition into fully developed grains. Although no direct experimental validation is provided in this study, the predicted increase in HAGB fraction with strain and the spatial redistribution of topological features qualitatively agree with prior observations in SPD-processed copper. Future efforts will focus on integrating EBSD or TEM-based measurements to directly validate the model's predictions and assess its generalizability to other materials and SPD configurations The topological analysis, characterized by Betti numbers (β_0, β_1, β_2), offers a deeper understanding of these changes. The global decrease in β_0 reflects the reduction in the isolated substructures of HAGBs. The stabilization of β_1 after the initial peak suggests that ring-shaped topological features across HAGB substructure remain stable during successive cycles. The increase in β_2, which correlates with the formation of new grains. Based on DCC-informed FE simulations and quantitative analysis of topology parameters, it is found that at the macroscale, HAGB fraction within the copper tube continuously increases with PTCAP cycles, reflecting the gradual evolution of the microstructure from subgrains to fully formed grains. Concurrently, β_0 decreases significantly, indicating that isolated structures progressively establish connections and form closed GB loops (as evidenced by β_1 increase), which subsequently evolve into stable new grains (as reflected by β_2 increase). This topological evolution pathway reveals the microstructural reconstruction mechanism underlying the transition from subgrain to grain structure during the PTCAP process. Analysis of topology evolution at different points of the copper tube highlights the important influence of spatially non-uniform plastic strain distribution on the rate of microstructure reconstruction during PTCAP. While pure copper was selected in this study as a model material due to its well-characterised recrystallisation behaviour and its relevance to SPD research, the proposed DCC-based framework is inherently applicable to other materials. The mathematical abstraction of microstructure as a discrete cell complex renders the model applicable to a broad range of materials. By adjusting material-specific inputs, such as constitutive parameters, deformation pathways, and GB mobility rules, the framework can be readily extended to simulate the microstructural evolution of various polycrystalline systems under comparable processing conditions. However, certain grain-scale phenomena, such as the explicit coalescence or splitting of grains, are currently represented implicitly through topological transitions within the network, rather than being tracked as discrete events. Future work will incorporate explicit GB migration rules and connectivity tracking to more accurately capture these localised phenomena.

This one-way coupling framework approach enabled the prediction of local equivalent strain distributions and provided initial insights into their influence on microstructural development. However, we acknowledge that even when different regions experience similar levels of equivalent strain, their resulting microstructures can differ significantly due to variations in strain path, rate, and local constraints. This highlights the need for developing a more advanced two-way coupling framework, where the evolving microstructure can in turn influence the local mechanical response. To address this, future work will explore two-way coupling strategies, through iterative updates of the FEA simulation informed by topology-aware constitutive models, and via concurrent multiscale approaches to more accurately capture the interplay between mechanics and microstructure.

Acknowledgement: The authors acknowledge the support from High Performance Computing Platform of Nanjing University of Aeronautics and Astronautics.

Funding Statement: The authors acknowledge the support from Outstanding Youth Fund of Jiangsu Province (BK20240077), Key Project (Provincial-Municipal Joint) of Jiangsu Province (BK20243044), Fundamental Research Funds for the Central Universities (NE2024001), National Youth Talents Program of China, and a project funded by the Priority Academic Program Development of Jiangsu Higher Education Institutions.

Author Contributions: Siying Zhu: Conceptualization; Methodology; Software; Validation; Formal Analysis; Investigation; Original Draft & Review & Editing; Project Administration; Supervision. Weijian Gao: Conceptualization; Methodology; Software; Validation; Formal Analysis; Investigation; Original Draft & Review & Editing. Min Yi: Conceptualization; Methodology; Formal Analysis; Writing—Original Draft & Review & Editing; Supervision; Project Administration; Funding Acquisition. Zhuhua Zhang: Conceptualization; Writing—Review & Editing; Supervision; Project Administration; Funding Acquisition. All authors reviewed the results and approved the final version of the manuscript.

Availability of Data and Materials: The datasets and code used or analyzed during the current study are available from the corresponding authors on reasonable request.

Ethics Approval: This article does not contain any studies with human participants or animals performed by any of the authors.

Conflicts of Interest: The authors declare no conflicts of interest to report regarding the present study.

List of Symbols and Abbreviations

∂_p	Boundary operators map p-chains to $(p-1)$-chains: $C_p \to C_{p-1}$
β_p	Betti numbers
χ	Euler characteristic
C_p	Collection of p-chains
k	Entropy constant
L_p	Combinatorial Laplacian map p-chains to p-chains: $C_p \to C_p$
$\mathcal{M}$	Collection of polyhedra
f	Fraction of high angle grain boundaries
S, S_J	Configurational entropy (Structural entropy)
T	Temperature
σ_p	p-cell
σ	Stress
ε	Accumulated plastic strain
CDRX	Continuous dynamic recrystallisation
DCC	Discrete cell complexes
FEM	Finite element method
GB	Grain boundary
GBE	Grain boundary engineering
GBN	Grain boundary network
HAGB	High angle grain boundary
LAGB	Low angle grain boundary
MEPP	Maximum entropy production principle
PTCAP	Parallel tube channel angular pressiong
QN	Quadruple node
RVE	Representative volume element
SPD	Severe plastic deformation
TJ	Triple junction
UFG	Ultra-fine grained

References

1. Valiev RZ, Islamgaliev RK, Alexandrov IV. Bulk nanostructured materials from severe plastic deformation. Prog Mater Sci. 2000;45(2):103–89. doi:10.1016/S0079-6425(99)00007-9.

2. Estrin Y, Vinogradov A. Extreme grain refinement by severe plastic deformation: a wealth of challenging science. Acta Mater. 2013;61(3):782–817. doi:10.1016/j.actamat.2012.10.038.
3. Harsha R, Kulkarni VM, Babu BS. Severe plastic deformation—a review. Mater Today Proc. 2018;5(10, Part 3):22340–9. doi:10.1016/j.matpr.2018.06.600.
4. Fattahi M, Hsu CY, Ali AO, Mahmoud ZH, Dang N, Kianfar E. Severe plastic deformation: nanostructured materials, metal-based and polymer-based nanocomposites: a review. Heliyon. 2023;9(12):e22559. doi:10.1016/j.heliyon.2023.e22559.
5. Zhang X, Gui Y, Lai M, Lu X, Gu J, Wang F, et al. Enhanced strength-ductility synergy of medium-entropy alloys via multiple level gradient structures. Int J Plast. 2023;164:103592. doi:10.1016/j.ijplas.2023.103592.
6. Demirtas M, Purcek G. Room temperature superplaticity in fine/ultrafine grained materials subjected to severe plastic deformation. Mater Trans. 2019;60(7):1159–67. doi:10.2320/matertrans.M2019015.
7. Edalati K, Hidalgo-Jiménez J, Nguyen TT, Sena H, Enikeev N, Rogl G, et al. Severe plastic deformation of ceramics by high-pressure torsion: review of principles and applications. Annu Rev Mater Res. 2025;55(1):89–124. doi:10.1146/annurev-matsci-080423-122701.
8. Sakai T, Belyakov A, Kaibyshev R, Miura H, Jonas JJ. Dynamic and post-dynamic recrystallization under hot, cold and severe plastic deformation conditions. Prog Mater Sci. 2014;60(1):130–207. doi:10.1016/j.pmatsci.2013.09.002.
9. Huang K, Logé RE. A review of dynamic recrystallization phenomena in metallic materials. Mater Des. 2016;111(8):548–74. doi:10.1016/j.matdes.2016.09.012.
10. Afifeh M, Hosseinipour SJ, Jamaati R. Nanostructured copper matrix composite with extraordinary strength and high electrical conductivity produced by asymmetric cryorolling. Mater Sci Eng A. 2019;763:138146. doi:10.1016/j.msea.2019.138146.
11. Gao Y, Guo T, Feng R, Qian D, Huang D, Zhang G, et al. High strength high conductivity copper prepared by C-ECAP and cryo-rolling. Mater Charact. 2024;208(9):113665. doi:10.1016/j.matchar.2024.113665.
12. Abbasi S, Momeni A, Lin Y, Jafarian H. Dynamic softening mechanism in Ti-13V-11Cr-3Al beta Ti alloy during hot compressive deformation. Mater Sci Eng A. 2016;665:154–60. doi:10.1016/j.msea.2016.04.056.
13. Sun Y, Zhang C, Feng H, Zhang S, Han J, Zhang W, et al. Dynamic recrystallization mechanism and improved mechanical properties of a near α high temperature titanium alloy processed by severe plastic deformation. Mater Charact. 2020;163:110281. doi:10.1016/j.matchar.2020.110281.
14. Randle V, Ralph B. Grain boundary structure and mechanical properties. Rev Phys Appl. 1988;23(4):501–12. doi:10.1051/rphysap:01988002304050100.
15. Engler O, Randle V. Introduction to texture analysis: macrotexture, microtexture, and orientation mapping. 2nd ed. Boca Raton, FL, USA: CRC Press; 2009. doi:10.1201/9781420063660.
16. Johnson OK, Schuh CA. The uncorrelated triple junction distribution function: towards grain boundary network design. Acta Mater. 2013;61(8):2863–73. doi:10.1016/j.actamat.2013.01.025.
17. Nguyen HD, Pramanik A, Basak A, Dong Y, Prakash C, Debnath S, et al. A critical review on additive manufacturing of Ti-6Al-4V alloy: microstructure and mechanical properties. Microstr Mech Prop, J Mater Res Technol. 2022;18(5):4641–61. doi:10.1016/j.jmrt.2022.04.055.
18. Schuh CA, Kumar M, King WE. Analysis of grain boundary networks and their evolution during grain boundary engineering. Acta Mater. 2003;51(3):687–700. doi:10.1016/S1359-6454(02)00447-0.
19. Frary M, Schuh CA. Grain boundary networks: scaling laws, preferred cluster structure, and their implications for grain boundary engineering. Acta Mater. 2005;53(16):4323–35. doi:10.1016/j.actamat.2005.05.030.
20. Liu T, Xia S, Li H, Zhou B, Bai Q. The highly twinned grain boundary network formation during grain boundary engineering. Mater Lett. 2014;133(10):97–100. doi:10.1016/j.matlet.2014.06.166.
21. Carter JL, Sosa JM, Shade PA, Fraser HL, Uchic MD, Mills MJ. The potential link between high angle grain boundary morphology and grain boundary deformation in a nickel-based superalloy. Mater Sci Eng A. 2015;640(4):280–86. doi:10.1016/j.msea.2015.05.031.
22. Huang Q, Zhu Q, Chen Y, Gong M, Li J, Zhang Z, et al. Twinning-assisted dynamic adjustment of grain boundary mobility. Nat Commun. 2021;12(1):6695. doi:10.1038/s41467-021-27002-3.

23. Liu Q, Fang L, Xiong Z, Yang J, Tan Y, Liu Y, et al. The response of dislocations, low angle grain boundaries and high angle grain boundaries at high strain rates. Mater Sci Eng A. 2021;822:141704. doi:10.1016/j.msea.2021.141704.
24. Liang C, Wang N, Chen Y, Jiang C, Wu G, Zhao Q, et al. Transition of low and high-angle grain boundaries during strain rate-induced dislocation storage and annihilation. Mater Charact. 2023;205(7):113284. doi:10.1016/j.matchar.2023.113284.
25. Chen MJ, Xie D, Fensin S, Hunter A, Li N, Zikry MA. Intergranular fracture, grain-boundary structure, and dislocation-density interactions in FCC bicrystals. Sci Rep. 2024;14(1):7454. doi:10.1038/s41598-024-72033-7.
26. Rohrer GS, Miller HM. Topological characteristics of plane sections of polycrystals. Acta Mater. 2010;58(10):3805–14. doi:10.1016/j.actamat.2010.03.028.
27. Wanner T, Fuller ER, Saylor DM. Homology metrics for microstructure response fields in polycrystals. Acta Mater. 2010;58(1):102–10. doi:10.1016/j.actamat.2009.08.061.
28. Zhu S, Borodin E, Jivkov AP. Topological characteristics of grain boundary networks during severe plastic deformations of copper alloys. Acta Mater. 2023;259(16):119290. doi:10.1016/j.actamat.2023.119290.
29. Bushuev O, Borodin E, Bodyakova A, Zhu S, Jivkov AP. Disorientation-based classification of mesostructures in severely deformed copper alloys. Acta Mater. 2025;286(4):120714. doi:10.1016/j.actamat.2025.120714.
30. Lowe TC, Valiev RZ. The use of severe plastic deformation techniques in grain refinement. JOM. 2004;56(10):64–8. doi:10.1007/s11837-004-0295-z.
31. Li M, Xu T. Topological and atomic scale characterization of grain boundary networks in polycrystalline and nanocrystalline materials. Prog Mater Sci. 2011;56(6):864–99. doi:10.1016/j.pmatsci.2011.01.002.
32. Pandey K, Poswal H. A new compact symmetric shear diamond anvil cell for in situ high-pressure-torsion studies. Rev Sci Instrum. 2023;95(5):053904. doi:10.1063/5.0172916.
33. Herbig M. Spatially correlated electron microscopy and atom probe tomography: current possibilities and future perspectives. Scr Mater. 2018;148:98–105. doi:10.1016/j.scriptamat.2017.11.031.
34. Gokuli M, Runnels B. Multiphase field modeling of grain boundary migration mediated by emergent disconnections. Acta Mater. 2021;217(4):117149. doi:10.1016/j.actamat.2021.117149.
35. Mishin Y. Stochastic model and kinetic monte carlo simulation of solute interactions with stationary and moving grain boundaries. II. Application to two-dimensional systems. Phys Rev Mater. 2023;7(6):063404. doi:10.1103/PhysRevMaterials.7.063404.
36. Zhao S, Zhang Y, Weber WJ. Stability of vacancy-type defect clusters in Ni based on first-principles and molecular dynamics simulations. Scr Mater. 2018;145:71–5. doi:10.1016/j.scriptamat.2017.10.003.
37. Pippan R, Wetscher F, Hafok M, Vorhauer A, Sabirov I. The limits of refinement by severe plastic deformation. Adv Eng Mater. 2006;8(11):1046–56. doi:10.1002/adem.200600133.
38. Pippan R, Scheriau S, Hohenwarter A, Hafok M. Advantages and limitations of hpt: a review. In: Materials science forum. Vol. 584, 2008. p. 16–21. doi:10.4028/www.scientific.net/MSF.584-586.16.
39. Zhu S, Borodin E, Jivkov AP. Triple junctions network as the key pattern for characterisation of grain structure evolution in metals. Mater Des. 2021;198(24):109352. doi:10.1016/j.matdes.2020.109352.
40. Zhu S. *In silico* grain boundary engineering by analysis on discrete complexes [Ph.D. thesis]. Manchester, UK: The University of Manchester; 2023.
41. Faraji G, Mashhadi MM, Kim HS. Tubular channel angular pressing (TCAP) as a novel severe plastic deformation method for cylindrical tubes. Mater Lett. 2011;65(19):3009–12. doi:10.1016/j.matlet.2011.06.039.
42. Faraji G, Babaei A, Mashhadi MM, Abrinia K. Parallel tubular channel angular pressing (PTCAP) as a new severe plastic deformation method for cylindrical tubes. Mater Lett. 2012;77:82–5. doi:10.1016/j.matlet.2012.03.007.
43. Kozlov D. Combinatorial algebraic topology. Vol. 21. Cham, Switzerland: Springer Science & Business Media; 2008. doi:10.1007/978-3-540-71962-5.
44. Boom PD, Kosmas O, Margetts L, Jivkov AP. A geometric formulation of linear elasticity based on discrete exterior calculus. Int J Solids Struct. 2022;236–237(1):111345. doi:10.1016/j.ijsolstr.2021.111345.
45. Berbatov K, Boom PD, Hazel AL, Jivkov AP. Diffusion in multi-dimensional solids using Forman's combinatorial differential forms. Appl Math Model. 2022;110(2):172–92. doi:10.1016/j.apm.2022.05.043.
46. Quey R. Neper: polycrystal generation and meshing; 2024. [cited 2025 Jul 1]. Available from: https://neper.info.

47. May JP. A concise course in algebraic topology. Vol. 38. Chicago, IL, USA: University of Chicago Press; 1999. p. 91199–9. doi: 10.1016/s0898-1221(99).
48. Cooke GE, Finney RL. Homology of cell complexes. Princeton, NJ, USA: Princeton University Press; 1967. doi:10.1515/9781400877751.
49. Mieghem PV. Graph spectra for complex networks. Cambridge, UK: Cambridge University Press; 2010. doi:10.1017/CBO9780511921681.
50. Weber M, Saucan E, Jost J. Characterizing complex networks with Forman-Ricci curvature and associated geometric flows. J Complex Netw. 2017;5(4):527–50. doi:10.1093/comnet/cnw030.
51. Friedman J. Computing betti numbers via combinatorial laplacians. Algorithmica. 1998;21(4):331–46. doi:10.1007/PL00009218.
52. Aktas ME, Akbas E, Fatmaoui AE. Persistence homology of networks: methods and applications. Appl Netw Sci. 2019;4(1):1–28. doi:10.1007/s41109-019-0179-3.
53. Agami S, Adler RJ. Modeling of persistent homology. Commun Stat-Theory Methods. 2020;49(20):4871–88. doi:10.1080/03610926.2019.1615091.
54. Spanier EH. Algebraic topology. Cham, Switzerland: Springer Science & Business Media; 1989. doi:10.1007/978-1-4684-9322-1.
55. Borodin EN, Morozova A, Bratov V, Belyakov A, Jivkov AP. Experimental and numerical analyses of microstructure evolution of Cu-Cr-Zr alloys during severe plastic deformation. Mater Charact. 2019;156(8):109849. doi:10.1016/j.matchar.2019.109849.
56. Ziegler H. An introduction to thermomechanics. Amsterdam, Netherlands: Elsevier; 2012.
57. Martyushev LM, Seleznev VD. Maximum entropy production principle in physics, chemistry and biology. Phys Rep. 2006;426(1):1–45. doi:10.1016/j.physrep.2005.12.001.
58. Martyushev LM. Entropy and entropy production: old misconceptions and new breakthroughs. Entropy. 2013;15(4):1152–70. doi:10.3390/e15041152.
59. Morozova A, Borodin E, Bratov V, Zherebtsov S, Belyakov A, Kaibyshev R. Grain refinement kinetics in a low alloyed Cu-Cr-Zr alloy subjected to large strain deformation. Materials. 2017;10(12):1394. doi:10.3390/ma10121394.
60. Lifshitz E, Pitaevskij L. Course of theoretical physics. Vol. 10. Oxford, UK: Physical kinetics; 1981.
61. Abd El Aal MI, Gadallah EA. Gadallah, parallel tubular channel angular pressing (PTCAP) processing of the Cu-20.7Zn-2Al tube. Materials. 2022;15(4):1469. doi:10.3390/ma15041469.
62. Wu S, Ju K, Duan C, Kong J. Dynamic mechanical properties and constitutive model of fine-grained T2 copper. Tool Eng. 2019;53(11):16–20. doi:10.3969/j.issn.1000-7008.2019.11.004.